Computational Performance at the Edge-of-Chaos in the Spin-Wave Interference-based Physical Reservoir Computing

Maki Nishimura[1,2], Daiki Nishioka[3], Wataru Namiki[1], Sota Hikasa[1,2], Ryo Iguchi[1], Kazuya Terabe[1] and Takashi Tsuchiya[1,2]*

[1]*Research Center for Materials Nanoarchitectonics (MANA), National Institute for Materials Science (NIMS), 1-1 Namiki, Tsukuba, Ibaraki, 305-0044, Japan*

[2]*Tokyo University of Science, 6-3-1 Niijuku, Katsushika, Tokyo, 125-8585, Japan*

[3]*International Center for Young Scientists (ICYS), National Institute for Materials Science (NIMS), 1-1 Namiki, Tsukuba, Ibaraki, 305-0044, Japan*

*Corresponding author email: TSUCHIYA.Takashi@nims.go.jp

Abstract

The edge of chaos (EoC) refers to a dynamical regime near the boundary between ordered and chaotic states, optimizing information processing in nonlinear dynamical systems. In physical reservoir computing (PRC), the EoC is crucial for high computational performance. Spin-wave interference–based PRC (SWI-PRC) demonstrated high performance, but the EoC's role hasn't been experimentally clarified. This study investigates a SWI-PRC system on a YIG single crystal, tuned by external magnetic field and input pulse interval adjustments. Using phase-space reconstruction and Lyapunov analysis, we evaluate the maximum Lyapunov exponent ($\lambda_{\max}$) and identify the EoC operating point. Additionally, we find an additional optimal regime on the chaotic side of the transition (the edge of chaos on the chaotic side). Performance evaluation through nonlinear waveform transformation tasks reveals up to 97% accuracy near the EoC, linking the $\lambda_{\max}$ to computational performance. These findings suggest that high performance in SWI-PRC stems from dynamically optimized points, offering design insights to enhance information-processing capabilities in edge computing applications.

Reservoir computing (RC) is a computational framework that exploits dynamical systems to project input signals into a high-dimensional state space, where the computational capability strongly depends on the underlying system dynamics. In RC, complex temporal tasks can be executed training only an output weight when the reservoir dynamics possess nonlinearity, high dimensionality, and short-term memory.[1-5] Because RC is inherently described as a dynamical system, its behavior can be characterized by various indicators, such as fixed-point structures, periodic orbits, correlation times, and spectral properties. However, these indicators do not necessarily capture how small input perturbations are amplified or attenuated over time, nor do they directly reflect the state separation capability essential for computation. In contrast, chaoticity quantified by the Lyapunov exponent provides a direct measure of dynamical stability, simultaneously characterizing two core requirements of RC: input separation and fading memory.

In RC systems with history, under conditions were sufficiently fast and continuous input is applied relative to the relaxation time, if the system is in an ordered state, differences in the initial input signal rapidly decay. Conversely, in a chaotic state, the system is sensitive to minute differences, which are amplified exponentially. At the boundary between these regimes, known as the edge of chaos (EoC), input differences are moderately amplified while past information is retained. This balance leads to an optimal trade-off between nonlinear transformation capability and memory retention. Previous theoretical studies, numerical simulations, and selected experimental systems have demonstrated that computational performance is maximized near the EoC.[6-15] Indeed, nanowire network reservoirs have been reported to exhibit peak task performance at the EoC.[10] More recently, the existence of a secondary performance peak on the chaotic side of the transition, has also been suggested in theoretical works.[16,17] Despite these advances, systematic experimental verification of the correlation between chaos and computational performance in real-device RC remains limited.

To address this challenge, an experimental platform is required in which nonlinearity and stability can be continuously controlled by experimental parameters, enabling the dynamical state to be swept from ordered to chaotic regimes within a single device. Physical reservoir computing (PRC), which implements RC using physical dynamics, provides a promising framework for this purpose by offering direct experimental access to the reservoir's dynamical states. A wide variety of physical systems have been explored for PRC, including electronic circuits,[18-20] electrochemical devices,[21-26] spintronic systems,[27-32] optical systems,[33-37] and ion-gating reservoirs.[38-45] Among these platforms, spin waves— collective spin excitations propagating in magnetic materials—are particularly attractive for experimentally investigating the relationship between chaos and computation, because their dynamics can be precisely controlled via external magnetic fields and input pulse conditions. In particular, the ferrimagnetic

material yttrium iron garnet (YIG) exhibits extremely low damping, enabling long-distance spin-wave propagation and rich interference effects. Spin-wave interference–based physical reservoir computing (SWI-PRC) implemented on YIG has been theoretically proposed and experimentally demonstrated to exhibit strong nonlinearity and short-term memory, properties well-suited for reservoir computing.[46-53] Spin-wave-based systems are also compatible with gigahertz-frequency operation and low power consumption when integrated with spintronic devices.[32] Furthermore, recent studies on spin systems using spin-torque oscillators have shown controlled transitions from ordered to chaotic dynamics, with chaos quantitatively evaluated using Lyapunov exponents,[28] highlighting the suitability of spin systems as experimental platforms for chaos analysis. Despite these advantages, although high computational performance has been reported in SWI-PRC implemented on YIG single crystals, the relationship between chaos and computational performance—particularly the experimental identification of the EoC—has not yet been systematically clarified.

In this study, we explore the EoC in SWI-PRC by controlling two external parameters: the applied static magnetic field and the input pulse interval to achieve high computational capability. The chaotic properties of the system are evaluated by calculating the Lyapunov spectrum from discrete-time series using a Jacobian matrix estimation method based on phase-space reconstruction, with the $\lambda_{\max}$ serving as a quantitative indicator of chaos. Furthermore, we elucidate the correlation between dynamical states and computational performance through nonlinear waveform transformation tasks and information processing capacity (IPC) analysis.

Figure 1(a) shows a schematic of the SWI-PRC system. A reservoir computing system consists of an input layer, a reservoir layer, and an output layer, where information processing is achieved by projecting input signals into a high-dimensional dynamical state space. In the echo state network (ESN) framework, only the output weights are trained, while the internal connections remain fixed.[1] The reservoir dynamics retain past input information and nonlinearly transform it into a high-dimensional feature space, enabling complex temporal processing using a simple linear readout. In PRC, the reservoir layer is implemented using physical dynamics and must satisfy three essential properties: short-term memory, nonlinearity, and high dimensionality.[1] For such dynamical systems, analyzing the underlying dynamics provides crucial insight into the stability and nonlinear characteristics of the time-series responses, which directly relate to their computational capability. Figure 1(b) shows an optical micrograph of the SWI-PRC device fabricated on a $Y_3Fe_5O_{12}$ (YIG) single crystal. Multiple coplanar waveguide antennas are patterned on the YIG surface to excite and detect propagating spin waves. In this study, the output from a single detector is analyzed to focus on the fundamental dynamical

behavior of the system. An external static magnetic field is applied perpendicular to the YIG surface (i.e., along the 111 direction of the YIG single crystal) to define the spin-wave propagation conditions, while pulsed electrical signals are used to excite spin waves through the input antenna. Two experimental parameters—the applied static magnetic field and the input pulse interval—are systematically varied to control the spin-wave dynamics. By tuning these parameters, the dynamical state of the SWI-PRC can be continuously modulated, providing an experimental platform for exploring the relationship between dynamical states and computational performance. Details of the device fabrication, measurement setup, electrical excitation and detection conditions, and vector network analyzer (VNA) characterization of the spin-wave propagation properties are provided in S1-S3 of the supplementary information.

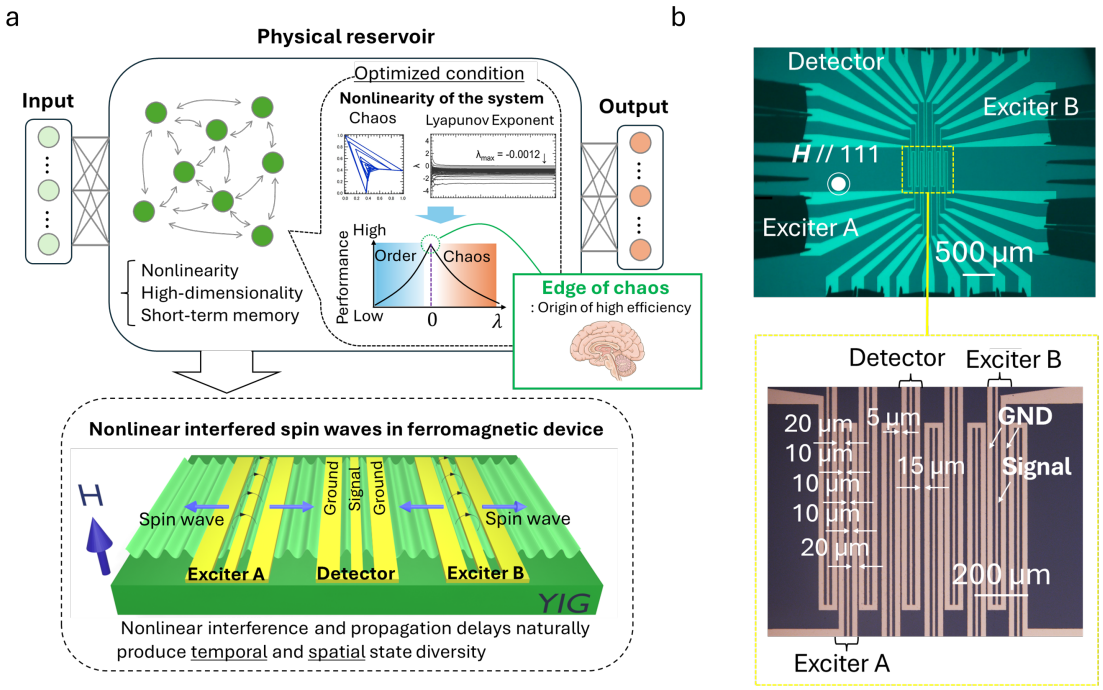

FIG.1 (a) Schematic of the SWI-PRC. (b) Optical microscope image of the YIG single crystal with the external magnetic field applied parallel to the 111 direction (top) and an enlarged view of the antenna structure (bottom).

To quantitatively evaluate the dynamical states of spin waves in the SWI-PRC, we calculated the Lyapunov spectrum using a Jacobian matrix estimation method based on phase-space reconstruction, and adopted its maximum value as the maximum Lyapunov exponent ($\lambda_{\max}$). This approach enables identification of transitions from ordered to chaotic dynamics and provides

a quantitative indicator of the system's dynamical state.[10)]

Figure 2(a) shows representative time-domain responses of the SWI-PRC measured under identical input conditions while varying the applied static magnetic field. The temporal waveforms are strongly modulated by the magnetic field, demonstrating that it serves as an effective control parameter for the underlying spin-wave dynamics. Figure 2(b) shows output responses measured at a fixed magnetic field of 178 mT with different input pulse intervals of 10 ns and 20 ns. Changing the pulse interval alters the decay and overlap of spin-wave responses to successive pulses, resulting in time series with different temporal correlation structures. These observations indicate that both the magnetic field and the pulse interval play crucial roles in controlling the system dynamics. In this study, a periodic triangular-wave signal is discretized to generate an input sequence $u(k)$, where k denotes discrete time, and each $u(k)$ is encoded into a pulse sequence that excites the spin-wave dynamics of the device. Using a virtual-node approach,[38,48)] the resulting continuous-time spin-wave responses within each pulse interval are uniformly sampled to construct reservoir states, allowing the system to be regarded as a discrete-time dynamical reservoir with states $X_i(k)$ (i = 1, 2, …, 50). Figure 2(c) shows a representative three-dimensional reconstructed phase-space map using the specific virtual node $X_i(k)$ and $X_i(k+1)$ together with the input signal. Sensitivity to initial conditions in dynamical systems can be quantified by tracking the temporal evolution of distances between nearby trajectories in reconstructed phase space. In chaotic systems, this sensitivity appears as exponential divergence, characterized by a positive maximum Lyapunov exponent $\lambda_{\max}$. Here, $\lambda_{\max}$ was evaluated from the reconstructed time series using a Jacobian-based Lyapunov spectrum estimation method.[12,38,54,55)] Details of the analysis procedure are provided in S4 of the supplementary information. For the phase-space reconstruction, an embedding dimension of D = 50 was used. To assess the validity of this choice, we evaluated the correlation dimension of the measured time series and estimated that an embedding dimension of approximately 11 or higher is sufficient to reconstruct the underlying dynamics. Since the embedding dimension used in this study is sufficiently larger than this estimated minimum, the reconstruction setting is considered appropriate for the estimation of the maximum Lyapunov exponent. Figures 2(d) and 2(e) show representative Lyapunov spectra corresponding to ordered (190 mT, 10 ns) and chaotic regimes (190 mT, 35 ns), respectively. The contrast results for the two conditions support that different temporal correlation structures of spin waves discussed in Fig. 2(b) give a strong impact on the dynamical state. Figure 2(f) summarizes the $\lambda_{\max}$ as a heat map as functions of the applied magnetic field and the input pulse interval. Blue regions indicate ordered dynamics with

negative $\lambda_{\max}$, whereas red regions correspond to chaotic dynamics with positive values. Ordered dynamics dominate for pulse intervals of 5–15 ns, while pronounced chaotic behavior emerges for pulse intervals of 20–40 ns. These results demonstrate that the dynamical state of the SWI-PRC can be continuously swept from ordered to chaotic regimes by controlling the applied magnetic field and the input pulse interval. The variation of the $\lambda_{\max}$ reflects the interplay between spin-wave relaxation time and the input pulse interval. The variation of $\lambda_{\max}$ can be attributed to differences in the excitation and relaxation processes of spin waves induced by periodic inputs. Specifically, as shown in Fig. 2(b), near the timing of the input pulses, the spin wave response is predominantly governed by spin waves directly excited by the input microwave field. In contrast, during the relaxation process, away from the input pulse timing, more diverse responses emerge due to interaction with persistent spin waves generated by previous inputs via nonlinear interactions. Therefore, under the condition of a fixed number of virtual nodes, when the pulse interval is short, the system dynamics are mainly governed by responses synchronized with the input signals, resulting in ordered behavior. As the interval becomes longer, components originating from the relaxation process become dominant in the node information, and the instability of the system becomes pronounced through the complex relaxation processes of the spin waves, leading to a transition to chaos. Generally, in the analysis of experimental data with significant noise, a positive $\lambda_{\max}$ can sometimes be erroneously observed, leading to a false identification of chaos. However, our results suggest that the observed $\lambda_{\max}$ trends are not primarily driven by noise. As seen in Fig. 2(b), longer pulse intervals result in lower signal amplitudes, where the relative contribution of noise to the reservoir states would theoretically be higher. If noise were the dominant factor for the positive $\lambda_{\max}$, $\lambda_{\max}$ would be expected to increase monotonically with the pulse interval. Contrary to this hypothesis, as shown in Fig. 2(f), the highest $\lambda_{\max}$ values occur at intermediate pulse intervals (e.g., ~20 ns at 178 mT and 198 mT) rather than at the longest intervals. This non-monotonic dependence contradicts the trend expected from noise-induced artifacts. Therefore, we conclude that the condition dependence of $\lambda_{\max}$ originates from the intrinsic differences in the excitation and relaxation processes induced by periodic inputs. As a result, the boundaries of these dynamic regions changed with the input pulse interval and magnetic field due to alterations in spin wave dispersion and damping, corresponding to the EoC.

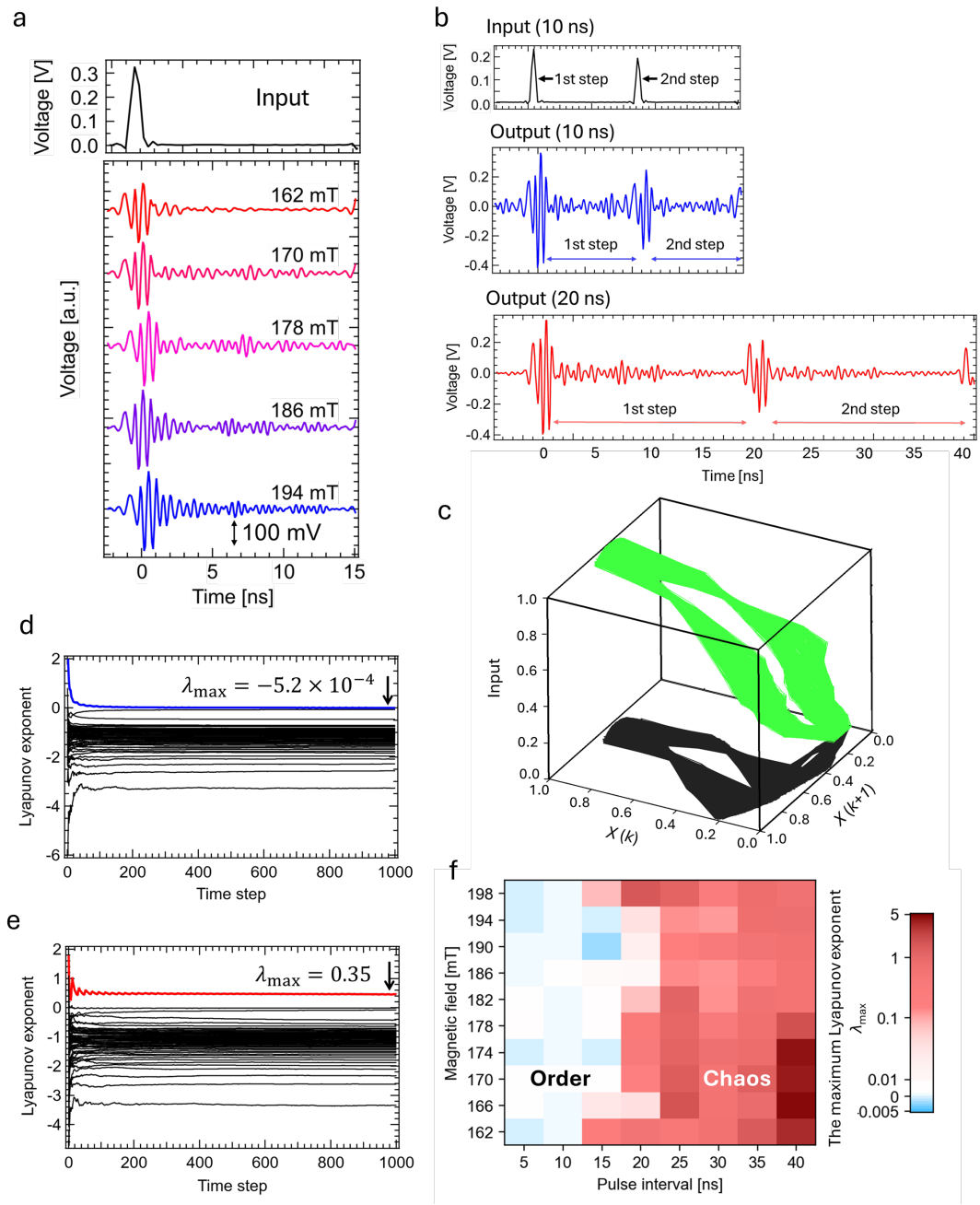

FIG. 2 (a) Time-domain responses of the SWI-PRC measured under identical triangular pulse input while varying the external magnetic field, demonstrating magnetic-field-induced modulation of the system dynamics. (b) Time-domain responses measured at different input pulse intervals (10 ns and 20 ns) under a fixed magnetic field of 178 mT, showing pulse-interval-dependent relaxation and temporal overlap of spin-wave responses. (c) Three-dimensional reconstructed phase-space map using virtual nodes $X(k)$ and $X(k+1)$ at an input pulse interval of 10 ns and a magnetic field of 170 mT (the green line). The projection of the trajectory onto the $X(k)$–$X(k+1)$ plane is shown by the black line on the base plane. (d,e) Representative Lyapunov spectra calculated by the Jacobian matrix estimation

method for (d) ordered and (e) chaotic dynamical regimes. (f) Heat map of the $\lambda_{\max}$ as functions of the external magnetic field and input pulse interval. Blue and red regions correspond to ordered (negative exponent) and chaotic (positive exponent) dynamics, respectively, revealing an edge-of-chaos regime in the SWI-PRC.

To directly examine the relationship between the dynamical state of a reservoir and its computational performance, it is advantageous to employ tasks whose performance optimization near the EoC has been established through both theoretical and experimental studies. In this work, we therefore adopt the nonlinear waveform transformation task as a representative benchmark.[10] The nonlinear waveform transformation task evaluates the linear and nonlinear transformation capabilities of a reservoir by measuring how accurately a desired target waveform can be generated from a triangular input waveform.[10,40,57] In this study, four target waveforms were considered: a sinusoidal wave, a square wave, a $\pi/2$ phase-shifted wave, and a second-harmonic (2f) wave. Previous studies have shown that the overall transformation accuracy for these tasks is maximized near the EoC.[10] A schematic of the task is shown in Fig. 3(a). The reservoir output $\boldsymbol{Y}(k)$ is obtained as a linear combination of the reservoir state $\boldsymbol{X}(k)=[X_1(k), X_2(k),\ldots, X_{50}(k)]$ with the readout weight vector $\boldsymbol{W}$, given by

$$\boldsymbol{Y}(k) = \boldsymbol{W}\boldsymbol{X}(k) \tag{1}$$

As in the Lyapunov analysis, the triangular input waveform was converted into a pulse sequence, and reservoir states were constructed using the same virtual-node approach. The readout weights $\boldsymbol{W}$ were trained using ridge regression to minimize the error between the reservoir output $\boldsymbol{Y}(k)$ and the target waveform $\boldsymbol{T}(k)$. Details of the training procedure are provided in S5. Figure 3(b) shows representative target waveforms and the corresponding outputs obtained from the SWI-PRC at an applied magnetic field of 190 mT and an input pulse interval of 10 ns. For all transformation tasks, the reservoir outputs show good agreement with the target waveforms. To clarify the relationship between the dynamical state and computational performance, the nonlinear waveform transformation task was performed for all measurement conditions, and the resulting accuracies are plotted as a function of the $\lambda_{\max}$ in Fig. 3(c). High accuracy is obtained for all tasks in the boundary region on the ordered side, where the $\lambda_{\max}$ is negative but close to zero. This result demonstrates that computational performance in the SWI-PRC is optimized near the EoC, consistent with previous reports.[10] Furthermore, after an initial degradation of performance in the chaotic regime, a secondary region of enhanced accuracy appears near the boundary on the chaotic side. In general, reservoir computing performance is governed by a balance between short-term memory and nonlinearity. In the ordered regime, the system tends to preserve memory but

provides limited nonlinear transformation, whereas in a strongly chaotic regime, nonlinear responses are enhanced but memory retention is degraded. The present results suggest that the regime near the edge of chaos on the chaotic side provides a balance between these two properties, allowing both sufficient memory and enhanced nonlinearity. This balance is advantageous for tasks requiring both temporal memory and nonlinear processing, leading to the observed improvement in computational performance. This behavior indicates the presence of a second optimal operating regime, originating from a dynamical state distinct from the primary order–chaos transition. Figure 3(d) compares the nonlinear waveform transformation accuracy at the EoC with those reported for other physical reservoir computing systems., which are few molecules reservoir,[57] all-solid-state electric double-layer transistors based on yttria-stabilized zirconia proton conductors (ASS-EDLTs),[40] and nanowire networks (NWNs) reservoirs with memristive junctions.[10] The performance of the present SWI-PRC is comparable to, or exceeds, that of previously reported physical reservoirs, demonstrating the effectiveness of dynamically optimized operation in SWI-PRC.

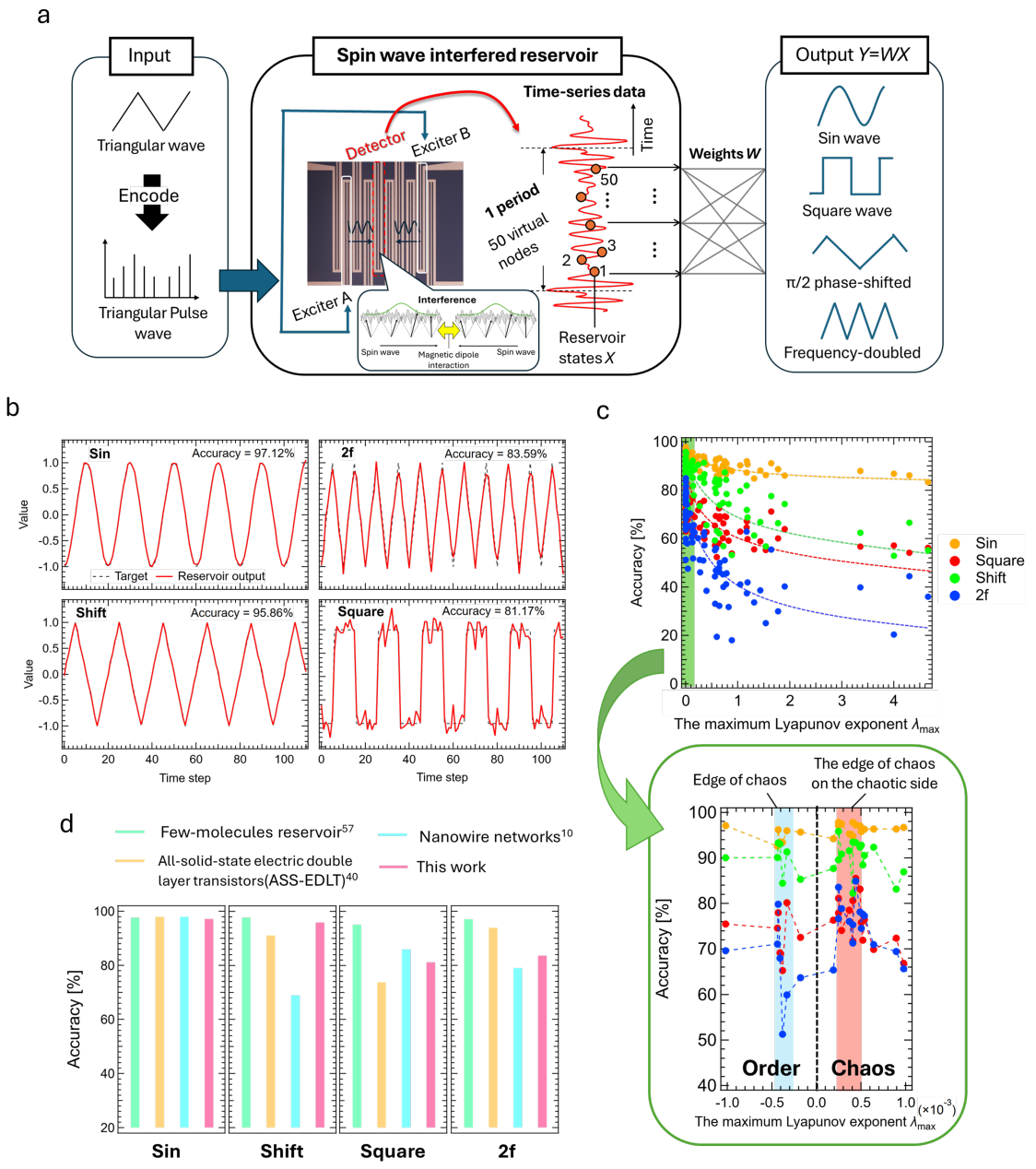

FIG.3 (a) Flow diagram of the nonlinear waveform transformation task in the SWI-PRC. (b) Comparison between the target waveforms and the waveforms predicted by the reservoir for sin, square, $\pi/2$ phase-shifted (Shift), and doubled-frequency (2f) waveforms, together with their corresponding accuracy. (c) Accuracy of transforming an input triangular waveform into different target waveforms as a function of the $\lambda_{\max}$. The results for the sin, $\pi/2$ phase-shifted (Shift), square, and doubled-frequency (2f) waveforms are shown in yellow, green, red, and blue, respectively. The upper panel shows the results over all measurement conditions, while the lower panel presents a magnified view around the $\lambda_{\max}$ of zero, corresponding to the boundary between ordered and chaotic regimes. The vertical line indicates $\lambda_{\max} = 0$. The vertical blue band on the ordered side represents

the edge of chaos, whereas the vertical red band on the chaotic side represents the edge of chaos on the chaotic side. (d) Comparison of the accuracies for the nonlinear waveform transformation task among various physical reservoir computing systems and the present study. From left to right, the results for the sin, $\pi/2$ phase-shifted (Shift), square, and doubled-frequency (2f) waveforms are shown. The green, yellow, blue, and red bars correspond to few-molecule reservoir computing,[57] all-solid-state electric double layer transistors (ASS-EDLTs),[40] memristor-junction nanowire networks (NWNs),[10] and this work, respectively.

In RC systems, both linear memory and nonlinear information processing coexist, enabling complex temporal computations. While linear memory represents the ability to retain past inputs, nonlinear information-processing capability is essential for performing higher-order transformations required for complex tasks.[58] To evaluate the computational capability of the SWI-PRC in a task-independent manner, we employed IPC analysis.[11,27,33,39,58] In IPC analysis, random input signals are applied to the reservoir, and the resulting time-series responses are used to quantify how many independent functions of the input can be reconstructed by a linear readout. The total IPC C_{tot} is defined as the sum of the capacities C_{n} associated with polynomial target functions of different orders,

$$C_{\mathrm{tot}} = \sum_{n} C_n \tag{2}$$

A larger C_{tot} indicates a higher computational capability across a broad class of tasks. Details of the IPC calculation procedure are provided in S6 of the supplementary information. Figure 4 compares the accuracy of the nonlinear waveform transformation task (Fig. 3(c), top) with the total IPC plotted as a function of the $\lambda_{\max}$ (bottom). As the $\lambda_{\max}$ approaches zero from the ordered side, the total capacity increases and reaches its maximum near the EoC regime. This behavior demonstrates that the enhancement of task performance near the EoC originates from an increase in the intrinsic information processing capability of the reservoir. Furthermore, when focusing on the vicinity of the zero $\lambda_{\max}$, C_{tot} exhibits a secondary increase on the chaotic side beyond a valley (decrease) at the order–chaos boundary. This trend coincides with the re-emergence of high accuracy observed in the nonlinear waveform transformation tasks and provides quantitative evidence for the existence of an additional optimal operating regime (the edge of chaos on the chaotic side). These results confirm that both the EoC and the edge of chaos on the chaotic side correspond to dynamically optimized states in which the SWI-PRC achieves enhanced information processing capability.

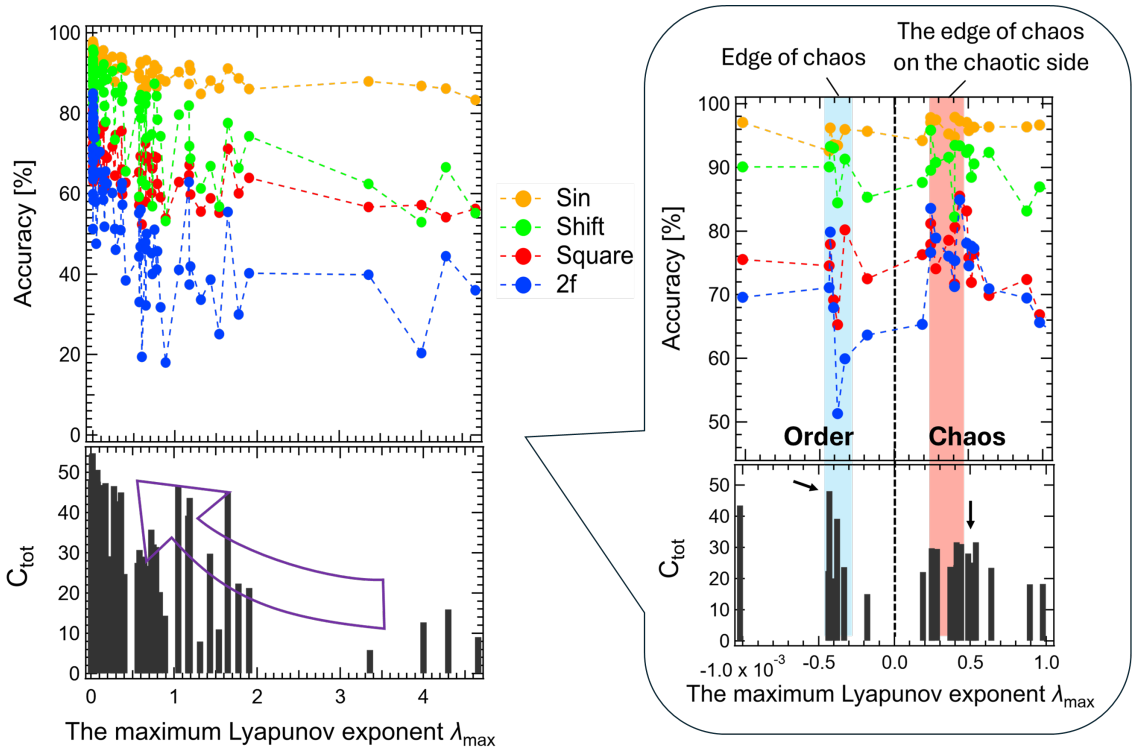

FIG.4 Accuracy of the nonlinear waveform transformation task (top) and the total IPC (bottom) as functions of the λ_{max}. The right panel shows a rescaled view focusing on the boundary region between the ordered and chaotic states near a zero λ_{max}. The vertical line indicates $\lambda_{max} = 0$, corresponding to the boundary between ordered and chaotic states. The blue band on the ordered side represents the edge of chaos, while the red band on the chaotic side represents the edge of chaos on the chaotic side.

In this study, we explored the EoC in SWI-PRC with a YIG single crystal, using experimental parameters to investigate the relationship between chaoticity and computational performance. We identified an EoC operating point at the boundary between ordered and chaotic dynamics, occurring at an input pulse interval of approximately 10 ns. In addition, we demonstrated that an additional optimal operating regime exists on the chaotic side of the transition. This regime, located near the edge of chaos on the chaotic side, represents a dynamically favorable state distinct from the primary order–chaos boundary and is likely characterized by the relaxation and interference properties of spin waves. Through computational performance evaluation on nonlinear waveform transformation tasks, we experimentally demonstrated a clear correlation between the dynamical states characterized by the λ_{max} and the computational performance of the SWI-PRC. In particular, high transformation accuracy was achieved near the EoC, indicating that the superior information processing capability of the SWI-PRC arises from dynamically optimized operating points. Furthermore, this work experimentally

reveals a clear correlation between the $\lambda_{\max}$, which characterizes the dynamical state, and computational performance in a SWI-PRC operating with gigahertz spin-wave dynamics, by controlling experimental parameters such as the input pulse interval and the applied magnetic field. These results demonstrate that optimal operating points for achieving high-speed and low-power information processing can be identified through dynamical-state control. Our findings provide practical design guidelines for spin-wave reservoir computing and highlight its potential for next-generation high-efficiency edge computing devices.

Acknowledgement

This research was in part supported by Japan Society for the Promotion of Science (JSPS) International Joint Research Program (JRP-LEAD with UKRI) Number: 20241712. A part of this work was supported by JSPS KAKENHI Grant Numbers JP25K17658. A part of this work was supported by "Advanced Research Infrastructure for Materials and Nanotechnology in Japan (ARIM)" of the Ministry of Education, Culture, Sports, Science and Technology (MEXT), proposal Number JPMXP1223NM5072.

Reference

1) H. Jaeger and H. Haas, *Science* **304**, 78 (2004).

2) W. Maass, T. Natschlager, and H. Markram, *Neural Comput.* **14**, 2531 (2002).

3) D. Verstraeten, B. Schrauwen, M. D'Haene, and D. Stroobandt, *Neural Networks* **20**, 391 (2007).

4) G. Tanaka, J. B. Heroux, R. Nakane, N. Kanazawa, S. Takeda, H. Numata, D. Nakano, and A. Hirose, *Neural Networks* **115**, 100 (2019).

5) S. Stepny, *Phys. D* **237**, 1157 (2008).

6) C. G. Langton, *Phys. D Nonlinear Phenomena* **42**, 12 (1990).

7) H. Sompolinsky, A. Crisanti, and H. J. Sommers, *Phys. Rev. Lett*. **61**, 259 (1988).

8) J. Boedecker, O. Obst, J. T. Lizier, N. M. Mayer, and M. Asada, *Theory Biosci.* **131**, 205 (2012).

9) N. Bertschinger and T. Natschlager, *Neural Compt.* **16**, 1413 (2004).

10) J. Hochstetter, R. Zhu, A. Loeffler, A. Diaz-Alvarez, T. Nakayama, and Z. Kuncic, *Nat. Commun.* **12**, 4008 (2021).

11) N. Akashi, T. Yamaguchi, S. Tsunegi, T. Taniguchi, M. Nishida, R. Sakurai, Y. Wakao, and K. Nakajima, *Phys. Rev. Res.* **2**, 043303 (2020).

12) K. Fukuda and Y. Horio, *Nonlinear Theory Appl. IEICE* **12**, 639 (2021).

13) D. Snyder, A. Goudazi, and C. Teuscher, *Phys. Rev. E* **87**, 042808 (2013).

14) J. P. Crutchfield and K. Young, *Phys. Rev. Lett.* **63**, 105 (1989).

15) T. L. Carroll, *arXiv:1906.03186* (2019).

16) J. Seifter and J. A. Reggia, *Artif. Life* **21**, 55 (2015).

17) T. Toyoizumi and L. F. Abbott, *Phys. Rev. E* **84**, 051908 (2011).

18) L. Appeltant, M. C. Sorano, G. van der Sande, J. Dankaert, S. Massar, J. Dambre, B. Schrauwen, C. R. Mirasso, and I. Fischer, *Nat. Commun.* **2**, 468 (2011).

19) C. Du, F. Cai, M. A. Zidan, W. Ma, S. H. Lee, and W. D. Lu, *Nat. Commun*. **8**, 2204 (2017).

20) S. Kan, K. Nakajima, Y. Takeshima,T. Asai, Y. Kuwahara, and M. A. Kasaya, *Phys. Rev. Appl.* **15**, 024030 (2021).

21) H. Tanaka, M. Akai-kasaya, A. TermechYousefi, L. Hong, L. Fu, H. Tamukoh, D. Tanaka, T. Asai, and T. Ogawa, *Nat. Commun*. **9**, 2693 (2018).

22) O. Srikimkaew, D. Banerjee, S. Azhari, Y. Usami, and H. Tanaka, *ACS Appl. Electron. Mater.* **6**, 688 (2023).

23) S. Kan, K. Nakajima, T. Asai, and M. A. Kasaya, *Adv. Sci*. **9**, 2104076 (2022).

24) S G. Koh, H. Shima, Y. Naitoh, H. Akinaga, and K. Kinoshita, *Sci. Rep*. **12**, 6958 (2022).

25) M. A. Kasaya, Y. Takeshima, S. Kan, K. Nakajima, T. Oya, and T. Asai, *Neuromorphic Comput. Eng*. **2**, 014003 (2022).

26) T. Shingu, H. Uchiyama, T. Watanabe, and Y. Ohno, *Carbon* **214**, 118344 (2023).

27) S. Tsunegi, T. Kubota, A. Kamimaki, J. Grollier, V. Cros, K. Yakushiji, A. Fukushima, S. Yuasa, H. Kubota, K. Nakajima, and T. Taniguchi, *Adv. Intell. Syst*. **5**, 2300175 (2023).

28) Y. Imai, K. Nakajima, S. Tsunegi, and T. Taniguchi, *Sci. Rep*. **12**, 21651 (2022)

29) N. Akashi, Y. Kuniyoshi, S. Tsunegi, T. Taniguchi, M. Nishida, T. Sakurai, Y. Wakao, K. Kawashima, and K. Nakajima, *Adv. Intell. Syst*. **4**, 2200123 (2022).

30) M. Romera, P. Talatchian, S. Tsunegi, F. A. Araujo, V. Cros, P. Bortolotti, J. Trastory, K.

Yakushiji, A. Fukushima, H. Kubota, S. Yuasa, M. Ernoult, D. Vodenicarevic, T. Hirtzlin, N. Locatelli, D. Querlioz, and J. Grollier, *Nature* **563**, 230 (2018).

31) J. Grollier, D. Querlioz, K. Y. Camsari, K. Evaerschor-Sitte, S. Fukami, and M. D. Stiles, *Nat. Electron.* **3**, 360 (2020).

32) J. Torrejon, M. Riou, F. A. Araujo, S. Tsunegi, G. Khalsa, D. Querlioz, P. Bortolotti, V. Cros, K. Fukushima, H. Kubota, S. Yuasa, M. D. Stiles, and J. Grollier, *Nature* **547**, 428 (2017).

33) M. Nakajima, K. Tanaka, and T. Hashimoto, *Commun. Phys*. **4**, 20 (2021).

34) F. Duport, A. Smerieri, A. Akrout, M. Healterman, and S. Massar, *Sci. Rep*. **6**, 22381 (2016).

35) F. Duport, B. Schneider, A. Smerieri, M. Healterman, and S. Massar, *Opt. Express* **20**, 22783 (2012).

36) M. Hermans, P. Antonik, M. Healterman, and S. Massar, *Phys. Rev. Lett*. **117**, 128301 (2016).

37) Y. Zhong, J. Tang, X. Li, B. Gao, H. Qian, and H. Wu, *Nat. Commun.* **12**, 408 (2021).

38) D. Nishioka, T. Tsuchiya, W. Namiki, M. Takayanagi, M. Imura, Y. Koide, T. Higuchi, and K. Terabe, *Sci. Adv*. **8**, eade1156 (2022).

39) D. Nishioka, H. Kitano, W. Namiki, S. Souma, K. Terabe, and T. Tsuchiya, *ACS Nano* **19**, 42 (2025).

40) M. Takayanagi, D. Nishioka, T. Tsuchiya, M. Imura, Y. Koide, T. Higuchi, and K. Terabe, *Mater. Today Adv.* **18**, 100393 (2023).

41) T. Wada, D. Nishioka, W. Namiki, T. Tsuchiya, T. Higuchi, and K. Terabe, *Adv. Intell. Syst*. **5**, 2300123 (2023).

42) K. Shibata, D. Nishioka, W. Namiki, T. Tsuchiya, T. Higuchi, and K. Terabe, *Sci. Rep*. **13**, 21060 (2023).

43) H. Kitano, D. Nishioka, K. Terabe, and T. Tsuchiya, *Appl. Phys. Express* **18**, 024501 (2025).

44) K. Terabe, T. Tsuchiya, T. Tsuruoka, H. Tanaka, I. Valov, J. K. Gimzewski, and T. Hasegawa, *Solid State Ionics* **430**, 116995 (2025).

45) W. Namiki, D. Nishioka, T. Tsuchiya, T. Higuchi, and K. Terabe, *Nano Lett*. **24**, 4383 (2024).

46) R. Nakane, G. Tanaka, and A. Hirose, *IEEE Access* **6**, 4462 (2018).

47) R. Nakane, A. Hirose, and G. Tanaka, *Phys. Rev. Appl*. **19**, 034047 (2023).

48) W. Namiki, D. Nishioka, Y. Yamaguchi, T. Tsuchiya, T. Higuchi, and K. Terabe, *Adv. Intell. Syst*. **5**, 2300228 (2023).

49) W. Namiki, D. Nishioka, Y. Nomura, T. Tsuchiya, K. Yamamoto, and K. Terabe, *Adv. Sci*. **12**, 2411777 (2025).

50) W. Namiki, D. Nishioka, T. Tsuchiya, and K. Terabe, *Neuromorph. Comput. Eng*. **4**, 024015 (2024).

51) W. Namiki, Y. Yamaguchi, D. Nishioka, T. Tsuchiya, and K. Terabe, *Mater. Today Phys*. **45**, 101465 (2024).

52) S. Iihama, Y. Koike, S. Mizukami, and N. Yoshinaga, *npj Spintronic*s **2**, 5 (2024).

53) S. Nagase, S. Nezu, and K. Sekiguchi, *Phys. Rev. Appl.* **22**. 024072 (2024).

54) S. Kumar, J. P. Strachan, and R. S. Williams, *Nature* **548**, 318 (2017).

55) M. Sano and Y. Sawada, *Phys. Rev. Lett.* **55**, 1082 (1985).

56) K. Fu, R. Zhu, A. Loeffler, J. Hochstetter, A. Diaz-Alvarez, A. Stieg, J. Gimzewski, T. Nakayama, and Z. Kuncic, *2020 International Joint Conference on Neural Networks* (*IJCNN*) (*IEEE*, 2020), pp. 1.

57) D. Nishioka, Y. Shingaya, T. Tsuchiya, T. Higuchi, and K. Terabe, *Sci. Adv*. **10**, eadk6438 (2024).

58) J. Dambre, D. Verstraeten, B. Schrauwen, and S. Massar, *Sci. Rep*. **2**, 514 (2012).

Supplementary Material

Computational Performance at the Edge-of-Chaos in the Spin-Wave Interference-based Physical Reservoir Computing

Maki Nishimura[1,2], Daiki Nishioka[3], Wataru Namiki[1], Sota Hikasa[1,2], Ryo Iguchi[1], Kazuya Terabe[1], and Takashi Tsuchiya[1,2]*

[1]*Research Center for Materials Nanoarchitectonics (MANA), National Institute for Materials Science (NIMS), 1-1 Namiki, Tsukuba, Ibaraki, 305-0044, Japan*
[2]*Tokyo University of Science, 6-3-1 Niijuku, Katsushika, Tokyo, 125-8585, Japan*
[3]*International Center for Young Scientists (ICYS), National Institute for Materials Science (NIMS), 1-1 Namiki, Tsukuba, Ibaraki, 305-0044, Japan*

*Corresponding author email: TSUCHIYA.Takashi@nims.go.jp

Supplementary section S1

YIG fabrication and material properties

The $Y_3Fe_5O_{12}$ (YIG) single crystal used in this study was a commercially available sample (Twoleads Co., Ltd.) oriented along the 111 plane and polished on both sides. The dimensions of the crystal were 7 mm × 7 mm × 0.5 mm. YIG is a ferrimagnetic material in which iron ions occupy two inequivalent crystallographic sites, Fe^{3+} at the 16a and 24d sites, with a population ratio of 2:3. Because the magnetic moments at these sites are oppositely aligned, the net magnetization originates from the excess magnetic moments at the Fe^{3+} 24d sites, giving rise to the spontaneous magnetization of YIG. The magnetization dynamics are described by the Landau–Lifshitz–Gilbert (LLG) equation, given by Eq. (S1).

$$\frac{d\boldsymbol{M}}{dt} = -\gamma\mu_0(\boldsymbol{M} \times \boldsymbol{H}_{\text{eff}}) + \frac{\alpha}{M_s}\left(\boldsymbol{M} \times \frac{d\boldsymbol{M}}{dt}\right) \quad \text{(S1)}$$

In the equation S1, γdenotes the absolute value of the gyromagnetic ratio, μ_0 is the vacuum permeability, $\alpha$is the Gilbert damping constant, and H_{eff} represents the effective magnetic field, defined as the sum of all effective fields arising from magnetic interactions and the externally applied magnetic field. The left-hand side of the equation describes the temporal evolution of the magnetization vector. The first term on the right-hand side represents the precessional motion of the magnetization around the magnetic field, while the second term corresponds to the damping of the precession. The combination of these two terms causes magnetization to spiral toward an

equilibrium state around the effective magnetic field. YIG is characterized by an exceptionally small Gilbert damping constant compared with other ferromagnetic materials, resulting in low spin-wave attenuation and a long spin-wave propagation length. For example, the spin-wave propagation length in Fe is approximately 0.5 μm, whereas that in a YIG single crystal reaches approximately 25,000 μm.[S1)] Owing to this long propagation length, spin-wave histories are readily preserved in YIG, leading to successive interference processes and the emergence of nonlinear spin-wave interference. Coplanar waveguide (CPW) antennas consisting of a 10-μm-wide signal line and two 20-μm-wide ground lines were fabricated using standard lithography techniques. Ti and Au were sequentially deposited as the antenna electrodes using an electron-beam evaporator. The edge-to-edge spacing between antennas was randomly arranged as either 5 μm or 15 μm, except for the edge antennas, for which the spacing was fixed at 10 μm. Although this device configuration is suitable for multidetectors experiments aimed at increasing reservoir dimensionality, in this study we used only the signal obtained from a single detection antenna in order to clarify the intrinsic dynamical behavior of spin-wave interference–based reservoir computing (SWI-PRC).

Supplementary section S2

Experimental setup

All experiments were performed using a high-frequency signal measurement system (RF probes and electromagnet) manufactured by Toei Scientific Industrial Co., Ltd. An external static magnetic field was applied perpendicular to the surface of the YIG single crystal, i.e., along the 111 crystallographic direction of the YIG. The sample temperature was maintained at room temperature (295 ± 1 K) throughout all measurements. The excitation antennas were connected via RF probes to an arbitrary waveform generator (Tektronix AWG5202), while the detection antenna was connected via RF probes to a mixed-signal digital oscilloscope (Tektronix MSO68B). Pulsed currents were applied using the arbitrary waveform generator to excite spin waves. Spin waves were excited by pulsed currents injected into the CPW antennas, generating radio-frequency magnetic fields, and detected as induced voltages via electromagnetic induction.[S2)]

The rise time, fall time, and on-time of the input pulses were all 320 ps. The maximum pulse voltage amplitude was set to 700 mV at the waveform generator output. During excitation, the input pulse signals were amplified by 21 dB using a radio-frequency amplifier before being applied to the CPW antenna. The induced voltage signals detected at the output antenna were further amplified by 38 dB prior to acquisition by the oscilloscope. To reduce noise components in the detected signals, signal averaging over 500 repetitions was performed. For the nonlinear waveform transformation task, the original triangular waveform $u(k) \in [0, 1]$ was encoded into

step voltage waveforms by converting each discrete input value into a pulse with a corresponding duration, ranging from 5 to 40 ns. Similarly, for IPC analysis, the original random waveform $u(k) \in [0, 0.5]$ was encoded into step voltage waveforms with pulse durations between 5 and 40 ns. Figure S1 illustrates the encoding process by comparing the original input waveforms and the corresponding pulse-encoded voltage waveforms used in the experiments. The converted random waveform consisted of 5,000 discrete time steps k. To eliminate residual effects from previously excited spin waves, a long interval of 4 μs was inserted between successive waveform sequences. The converted triangular and random waveforms were then applied to the SWI-PRC. The voltage signals obtained after propagation through the reservoir were recorded as time-series data and used to perform each computational task.

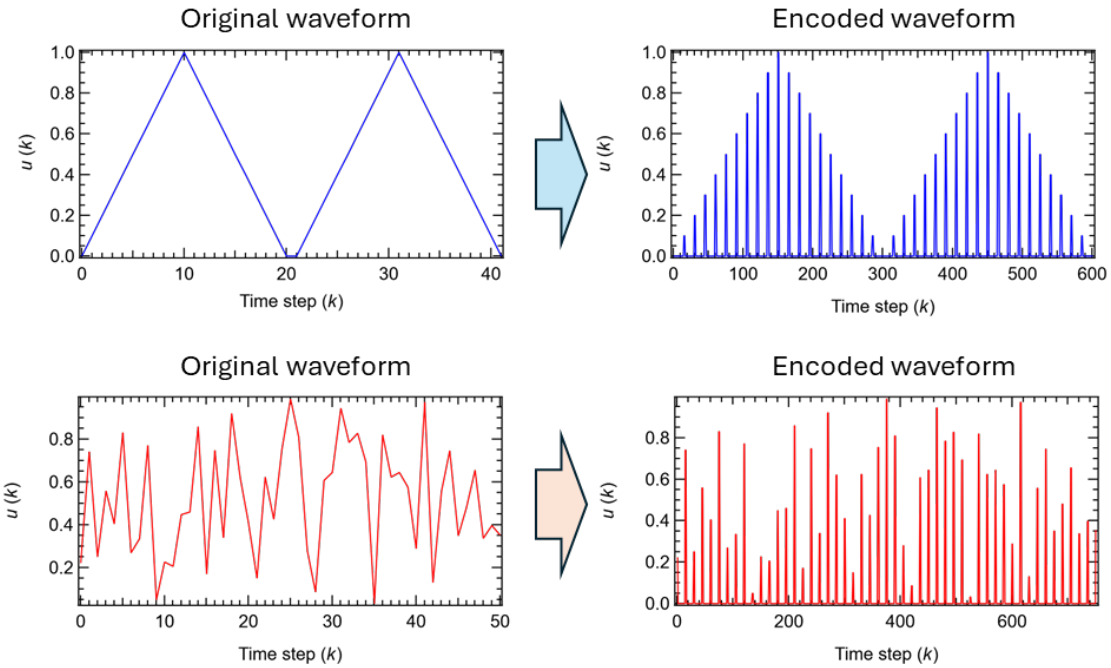

FIG. S1 Encoding of input waveforms into pulse voltage signals. (upper) Original triangular waveform $u(k) \in [0, 1]$ and the corresponding pulse-encoded voltage waveform used for the nonlinear waveform transformation task (upper). Original random waveform $u(k) \in [0, 1]$ and the corresponding pulse-encoded voltage waveform used for IPC analysis (bottom).

Supplementary section S3

VNA analysis

Spin waves are excited by the injected pulsed current; therefore, the spin-wave wave number k is determined by the geometrical configuration of the antennas.[S3)] To characterize the spin-wave propagation properties in the present device, vector network analyzer (VNA)

measurements were performed. Figure S2 shows the frequency–magnetic-field dependence of the excited spin waves obtained from the VNA measurements. Regions with strong spin-wave intensity are indicated in white, while horizontal lines originate from signals unrelated to spin-wave excitation. Owing to the antenna geometry, multiple wave-number peaks appear in the current spectrum; accordingly, three representative wave numbers are considered in this study. When a magnetic field is applied perpendicular to the film plane, the spin-wave frequency can be described by the spin-wave dispersion relation, given as follows :[S4)]

$$f = \gamma\mu_0\sqrt{(H - H_a)\{(H - H_a) + M(1 - \frac{1 - e^{-kd}}{kd})\}} \quad \text{(S2)}$$

Here, f, γ, μ_0, H, H_a, M, k, and d denote the frequency, gyromagnetic ratio, vacuum permeability, applied external magnetic field, magnetic anisotropy field, saturation magnetization, wave number, and thickness of the YIG single crystal, respectively. Except for H, these parameters are determined by the antenna geometry and the magnetic material properties. The gyromagnetic ratio was fixed at $\gamma = 28$ GHz/T. As shown in Fig. S2, three bright dispersion branches are observed, indicated by the blue, red, and green dashed lines. By fitting these branches using Eq. (S2), the values of $\mu_0 M$ and $\mu_0 H_a$ were determined to be (189 ± 2.5) mT and (153 ± 3.9) mT, respectively. Using these parameters, the corresponding wave numbers were calculated to be $k_1 = 0.104\ \mu\text{m}^{-1}$, $k_2 = 0.307\ \mu\text{m}^{-1}$, and $k_3 = 0.631\ \mu\text{m}^{-1}$. These values are in good agreement with those reported in previous studies, confirming the validity of the fitting procedure. In the present experiments, the input waveform generated by the arbitrary waveform generator has a characteristic frequency of approximately 1.1 GHz. From Fig. S2, the corresponding resonance condition is therefore identified to be around an external magnetic field of approximately 180 mT.

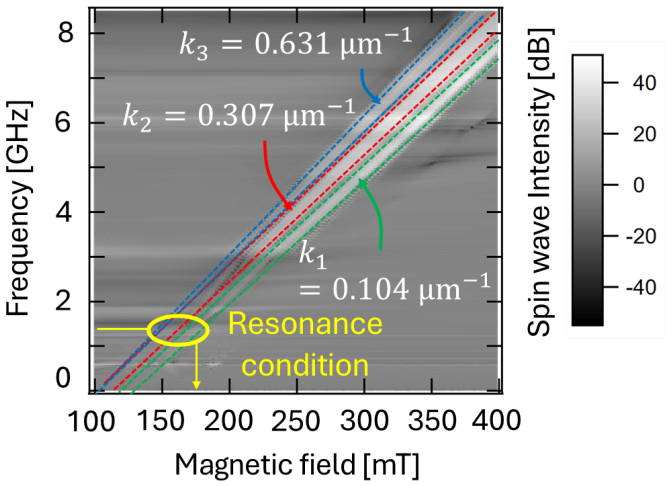

FIG. S2 Magnetic-field dependence of the resonance frequency of spin waves. The blue, red, and green dashed lines represent the fitting curves.

Supplementary section S4

S4.1 Virtual-node construction

The detected voltage waveform contains two distinct components: (i) a fast spike-like response originating from electromagnetic induction associated with the rising and falling edges of the input pulses, and (ii) a slower relaxation response arising from spin-wave propagation and interference in the YIG medium. Because the former directly reflects the input pulse waveform and does not represent intrinsic spin-wave dynamics, it was excluded from the reservoir-state construction. After removing the electromagnetic spike components, a time window dominated by the spin-wave response was identified for each input pulse step. From this window, 50 sampling points were uniformly extracted at equal time intervals and treated as independent virtual nodes, following established approaches in physical reservoir computing.[S5,S6] This procedure ensures that the reservoir states predominantly reflect nonlinear and history-dependent spin-wave dynamics rather than direct electromagnetic coupling. As a result, the reservoir state at discrete time step k is represented as a 50-dimensional vector composed of the sampled spin-wave responses within one input pulse step.

In this study, the original triangular waveform was encoded into a pulse sequence consisting of 20 discrete steps per period, and a total of 1,100 periods of the triangular pulse waveform were applied to the device. To ensure stationary dynamical behavior, the initial 100 periods were discarded, and the remaining 1,000 periods were used for subsequent analysis. At each discrete time step, the reservoir state constructed from the 50 virtual nodes enabled the

formulation of the system as a discrete-time dynamical system. The dynamical behavior of the reservoir was evaluated by quantifying the evolution of infinitesimal differences between nearby states using the maximum Lyapunov exponent calculated via the Jacobian matrix estimation method, which provides a quantitative measure of sensitivity to initial conditions and transitions between ordered and chaotic regimes.

S4.2 Jacobian matrix estimation method for Lyapunov exponent analysis

To evaluate the chaoticity of the reservoir computing system investigated in this study, we employed the Lyapunov spectrum, which serves as a quantitative measure of orbital instability. The SWI-PRC was treated as a discrete-time dynamical system for the purpose of this analysis The Lyapunov exponents are defined as quantities calculated from the Jacobian matrix of the system and can be expressed as follows :[S5-S7)]

$$\lambda = \lim_{T\to\infty} \frac{1}{T} \sum_{t=1}^{T} \ln\left|g'(x(t))\right| \tag{S3}$$

Here, t and $g'(*)$ denote the iteration time and the derivative of the mapping function $g(*)$, respectively. The quantity λ is referred to as the Lyapunov exponent: a positive value of λ indicates that nearby trajectories diverge exponentially, whereas a negative value indicates that nearby trajectories converge asymptotically. Although Lyapunov exponents can be formally defined using an explicit mapping function, such an approach is not suitable for experimental systems in which the governing equations are unknown. Therefore, in this study, the Lyapunov exponents were evaluated using the Jacobian matrix estimation method. In this method, the Jacobian matrix is estimated from time-series data by analyzing the local structure of the attractor reconstructed in an m-dimensional phase space. Specifically, we consider an m-dimensional hypersphere of radius ε centered at a point $\mathbf{v}(t)$ on the attractor at time t. Let $\mathbf{v}(k_i)(i = 1,2,\dots,M)$ denote neighboring points on the attractor located within this hypersphere. The displacement vectors $\boldsymbol{\mu}_i$ from $\mathbf{v}(t)$ to $\mathbf{v}(k_i)$ are defined as

$$\boldsymbol{\mu}_i = \boldsymbol{v}(k_i) - \boldsymbol{v}(t) \tag{S4}$$

Furthermore, the displacement vector $\mathbf{z}_i$ after a time interval $s$is obtained as follows. When the radius ε of the neighborhood and the time interval s are sufficiently small, the time evolution of the displacement vector can be approximated by a linear mapping, as shown on the right-hand side:

$$\mathbf{z}_i = \boldsymbol{v}(k_i + s) - \boldsymbol{v}(t + s) \approx \hat{\boldsymbol{J}}(t)\boldsymbol{\mu}_i \tag{S5}$$

From this relation, the Jacobian matrix can be estimated as follows:

$$\hat{\boldsymbol{J}}(t) = \mathbf{z}_i \boldsymbol{\mu}_i^T (\boldsymbol{\mu}_i \boldsymbol{\mu}_i^T)^{-1} \tag{S6}$$

By performing QR decomposition of the Jacobian matrix at time t, we obtain

$$\hat{\boldsymbol{J}}(t)\boldsymbol{Q}_t = \boldsymbol{Q}_{t+1}\boldsymbol{R}_{t+1} \tag{S7}$$

As a result, the Lyapunov exponent $\lambda_i (i = 1,2,\dots,m)$ is calculated as

$$\lambda_i = \lim_{T\to\infty} \frac{1}{2T} \sum_{k=1}^{2T} \log\left|\boldsymbol{R}_k^{ii}\right| \tag{S8}$$

Here, R_k^{ii} denotes the i-th diagonal element of the upper triangular matrix $\mathbf{R}_k$. The Lyapunov exponents λ_i obtained in this manner are calculated for each dimension of the reconstructed state space to form the Lyapunov spectrum. By examining the maximum Lyapunov exponent after sufficiently long-time evolution, the degree of nonlinearity and chaoticity of the system can be quantitatively evaluated.

Supplementary section S5

Nonlinear waveform transformation task

Here, we describe the nonlinear waveform transformation task performed to evaluate the nonlinear transformation capability of the SWI-PRC system. In this task, a triangular waveform is used as the input, and four types of target waveforms $T(k)$ are considered: a sinusoidal waveform (Sin), a square waveform (Square), a $\pi/2$ phase-shifted triangular waveform (Shift), and a second-harmonic triangular waveform (2f). The input triangular waveform was converted into a voltage pulse sequence and applied to the SWI-PRC. The pulse interval for each step was varied from 5 to 40 ns, and one period of the triangular waveform consisted of 20 steps. A total of 1,100 periods of the triangular waveform were input to the reservoir; the initial 100 periods corresponding to transient dynamics were discarded, and the remaining 1,000 periods were used for computation. Previous studies have reported that, in SWI-PRC using YIG single crystals, 50 virtual nodes are extracted per pulse step for task evaluation. Following this approach, in the present study, 50 virtual nodes were extracted at each step to construct the reservoir state vector $\boldsymbol{x}(k)$. The reservoir output $y(k)$ was obtained by a linear combination of the reservoir state vector weighted by the readout weight matrix $\boldsymbol{W}$, as described by Eq. (1) in the main text. Here, k denotes the discrete time step. The weight matrix $\boldsymbol{W}$ was trained using ridge regression such that the reservoir output $y(k)$ reproduces the target waveform $T(k)$. The cost function J used for ridge regression is given by Eq. (S9) below.

$$J(W) = \frac{1}{2}\sum_{k=1}^{L}[T(k) - Y(k)]^2 + \frac{\lambda}{2}\sum_{i=1}^{N} w_i^2 \tag{S9}$$

Here, $L(=40)$ and $\lambda(=10^{-6})$ denote the data length and the regularization parameter, respectively. The weight vector $\boldsymbol{W}$ that minimizes the cost function J is given by Eq. (S10) as

follows:

$$\widehat{\boldsymbol{W}} = \boldsymbol{Y}\boldsymbol{X}^T(\boldsymbol{X}\boldsymbol{X}^T + \lambda \boldsymbol{I})^{-1} \quad \text{(S10)}$$

Here, $\mathbf{T} = [T(1), T(2), \ldots, T(L)]$, $\mathbf{X} = [\mathbf{x}(1), \mathbf{x}(2), \ldots, \mathbf{x}(L)]$, and $\mathbf{I} \in \mathbb{R}^{N \times N}$ denote the target output matrix, the reservoir state matrix, and the identity matrix, respectively. The readout network and the trained weights were stored and executed on a personal computer. By training the readout weights, the output data $T(k)$ can be obtained from the reservoir states. For all transformation tasks, the length of the training data was set to 800 periods × 20 steps. The computational performance of the reservoir was evaluated using the prediction accuracy calculated from the normalized mean square error (NMSE) between the output waveform and the target waveform.[S8-S11)]

$$\text{Accuracy} = 1 - \sqrt{\text{NMSE}} \quad \text{(S11)}$$

$$\text{NMSE} = \frac{\sum_{k=1}^{L}[T(k) - y(k)]^2}{\sum_{k=1}^{L} T^2(k)} \quad \text{(S12)}$$

Supplementary section S6

Information Processing Capability

Here, we describe the method used to calculate the information processing capability (IPC). IPC quantifies the nonlinearity and memory capacity of a reservoir computing (RC) system by evaluating the reconstruction accuracy of target signals from the reservoir states. The target data $y_m(k)$ are defined as orthogonal polynomials that span all linear and nonlinear combinations of the input signals.

$$y_m(k) = \prod_{d=0}^{D} P_{n_{m,d}}[u(k-d)] \quad \text{(S13)}$$

Here, $P_{n'}$ denotes an orthogonal polynomial of order $n' = 1,2,3, \ldots$. Although Legendre polynomials are commonly used for IPC analysis, in this study we employed polynomials generated by the Gram–Schmidt orthogonalization method in order to minimize the influence of the limited data size.[S12, S13)] In this formulation, m, d, and D represent the polynomial index, the delay, and the maximum delay, respectively. The input signal $u(k)$ is a uniformly distributed random sequence. Equation (S14) defines the mean square error (MSE). The component-wise capacity C_m for a given index m is calculated based on the MSE for reconstructing $y_m(k)$ from the reservoir states $\mathbf{X}(k)$ obtained by driving the reservoir with the input $u(k)$, as expressed in Eq. (S15).

$$\text{MSE} = \frac{1}{L}\sum_{k=1}^{L}[y_m(k) - y(k)]^2 \quad \text{(S14)}$$

$$C_m = 1 - \frac{\mathrm{MSE}}{\langle y_m^2 \rangle} \tag{S15}$$

Here, $\langle y_m^2 \rangle$ is defined as $\langle y_m^2 \rangle = \frac{1}{L}\sum_{k=1}^{L} y_m^2(k)$. The total information processing capacity C_{tot} is defined as the sum of the individual capacities C_n.

$$C_{\mathrm{tot}} = \sum_{m=1}^{M} C_m \tag{S16}$$

Here, M denotes the total number of indices determined by all combinations of polynomial order and delay. In addition, the capacity for each order is calculated as the sum of the capacities of all target functions having the same total order n.

$$C_n = \sum\nolimits_{m(n)} C_m \tag{S17}$$

Here, $m(n)$ denotes the set of all indices corresponding to the total order n. Accordingly, the total capacity C_{tot} can also be expressed as in Eq. (2) of the main text.

Reference

S1) A. Mahmoud, F. Ciubotaru, F. Vanderveken, A. V. Chumak, S. Hamdioui, C. Adelmann, and S. Cotofana, *J. Appl. Phys*. **128**, 161101 (2020).

S2) W. Namiki, D. Nishioka, Y. Yamaguchi, T. Tsuchiya, T. Higuchi, and K. Terabe, *Adv. Intell. Syst*. **5**, 2300228 (2023).

S3) S S. Kalarickal, P. Krivosik, M. Wu, C E. Patton, M L. Schneider, P. Kabos, T. J. Silva, and J P. Nibarger, *J. Appl. Phys*. **99**, 093909 (2006).

S4) V. Vlaminck and M. Bailleul, *Phys. Rev*. B **81**, 014425 (2010).

S5) K. Fukuda and Y. Horio, *Nonlinear Theory Appl. IEICE* **12**, 639 (2021).

S6) M. Sano and Y. Sawada, *Phys. Rev. Lett.* **55**, 1082 (1985).

S7) D. Nishioka, T. Tsuchiya, W. Namiki, M. Takayanagi, M. Imura, Y. Koide, T. Higuchi, and K. Terabe, *Sci. Adv*. **8**, eade1156 (2022).

S8) J. Hochstetter, R. Zhu, A. Loeffler, A. Diaz-Alvarez, T. Nakayama, and Z. Kuncic, *Nat. Commun.* **12**, 4008 (2021).

S9) K. Fu, R. Zhu, A. Loeffler, J. Hochstetter, A. Diaz-Alvarez, A. Stieg, J. Gimzewski, T. Nakayama, and Z. Kuncic, *2020 International Joint Conference on Neural Networks* (*IJCNN*) (*IEEE*, 2020), pp. 1.

S10) M. Takayanagi, D. Nishioka, T. Tsuchiya, M. Imura, Y. Koide, T. Higuchi, and K. Terabe, *Mater. Today Adv.* **18**, 100393 (2023).

S11) D. Nishioka, Y. Shingaya, T. Tsuchiya, T. Higuchi, and K. Terabe, *Sci. Adv*. **10**, eadk6438 (2024).
S12) D. Nishioka, H. Kitano, W. Namiki, S. Souma, K. Terabe, and T. Tsuchiya, *ACS Nano* **19**, 42 (2025).
S13) T. Kubota, H. Takahashi, K. Nakajima, *Phys. Rev. Res*., **3** (4), 43135 (2021).